

A scanning transmon qubit for strong coupling circuit quantum electrodynamics

W. E. Shanks,^{1,*} D. L. Underwood,¹ and A. A. Houck¹

¹*Department of Electrical Engineering, Princeton University, Olden Street, Princeton, NJ 08550*

(Dated: August 18, 2021)

MAIN BODY

Like a quantum computer designed for a particular class of problems, a quantum simulator enables quantitative modeling of quantum systems that is computationally intractable with a classical computer. Quantum simulations of quantum many-body systems have been performed using ultracold atoms¹ and trapped ions² among other systems. Superconducting circuits have recently been investigated as an alternative system in which microwave photons confined to a lattice of coupled resonators act as the particles under study with qubits coupled to the resonators producing effective photon-photon interactions³. Such a system promises insight into the nonequilibrium physics of interacting bosons but new tools are needed to understand this complex behavior. Here we demonstrate the operation of a scanning transmon qubit and propose its use as a local probe of photon number within a superconducting resonator lattice. We map the coupling strength of the qubit to a resonator on a separate chip and show that the system reaches the strong coupling regime^{4, 5} over a wide scanning area.

Over the past decade, the study of quantum physics using superconducting circuits has seen rapid advances in sample design and measurement techniques^{6–8}. A great strength of superconducting qubits compared to other promising candidates is that they are fabricated using standard lithography procedures which allow fine tuning of qubit properties and make scaling up the fabrication to devices with many qubits straightforward. Circuit quantum electrodynamics (CQED) is an active branch of quantum physics research in which one or more qubits are strongly coupled to a superconducting coplanar waveguide resonator (CPWR) which is used to control and readout the state of the qubits^{5, 9}. A prerequisite for most interesting CQED applications is that the system reach the strong coupling regime in which the rate at which the qubit and the resonator exchange an excitation exceeds the excitation decay rate.

In addition to the CQED architecture's promise as a quantum computing platform, recent theoretical work has focused on using a CQED lattice, a network of coupled resonators each coupled to its own qubit, as a nonequilibrium quantum simulator³. One particularly interesting prediction for CQED lattice systems is a crossover from a superfluid-like state to an insulating state as, for example, the coupling between the qubits and their resonators is increased^{10–12}, similar to the superfluid-

Mott insulator quantum phase transition which has been observed in ultracold atom systems^{1, 13}. More exotic phenomena including analogs of the fractional¹⁴ and anomalous¹⁵ quantum Hall effects and of Majorana physics¹⁶ have also been considered. However, while preliminary steps have been taken to build such a CQED lattice system¹⁷, both establishing and probing its expected many-body states remain major experimental challenges.

The simplest method of probing a microwave circuit is to measure transmission between two of its ports. However, in the case of a CQED lattice such a measurement gives only limited insight into the detailed behavior of photons in the interior. Additional information could be obtained by measuring transmission while locally perturbing the interior of the sample, as has been done to image the coherent flow of electrons in two-dimensional

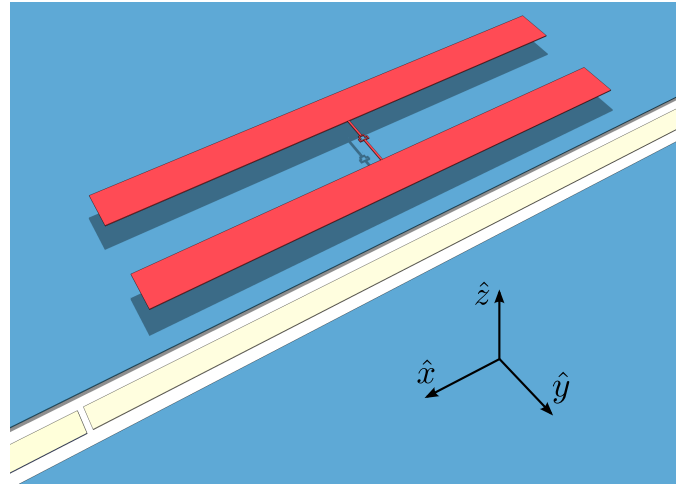


Figure 1. Scanning transmon qubit. The qubit (red) is composed of two $40 \times 500 \mu\text{m}$ aluminum islands separated by a $60 \mu\text{m}$ gap and connected by a thin wire containing a Josephson tunnel barrier. In the qubit discussed here, the tunnel barrier is formed by two aluminum oxide barriers in the two arms of a loop in the middle of the wire. The qubit is pictured $11 \mu\text{m}$ above a portion of a CPWR. The resonator's center pin (yellow) is $21 \mu\text{m}$ wide and is separated from the surrounding ground plane (blue) by $12 \mu\text{m}$ gaps. The ends of the resonator are formed by gaps in the center pin like the one shown in the figure. The resonator has a length of $7,872 \mu\text{m}$ which corresponds to a half-wave resonance of 7.6 GHz in the absence of the qubit. The resonator center pin has no curves in over half its length, so that the qubit remains aligned as it scans over this part of the resonator. To make them more visible, the qubit and resonator have been thickened, but all other dimensions are to scale with the samples discussed here.

electron gas systems^{18, 19}. This local perturbation requires a new scanning probe tool, such as the one demonstrated here. Besides just perturbing the lattice, a scanning probe qubit can be used to measure the photon number of individual lattice sites following a protocol used to measure photons in non-scannable cavities²⁰. One benefit of a scanning qubit in this case is its ability to measure the photon number of interior lattice sites. Measurements of outer resonators, those most easily accessed by a measurement circuit fabricated on the same chip as the lattice, would be difficult to interpret due to edge effects.

While our primary focus is on using the scanning qubit in the context of CQED lattice-based quantum simulation, we note that scanning qubits have been studied previously for other applications. Scanning nitrogen-vacancy (NV) center qubits in diamond have been demonstrated to be sensitive local probes of magnetic field^{21, 22}. A diamond NV center has also been coupled to a scanning photonic crystal cavity²³. While this experiment did not reach the strong coupling regime, the scanning cavity enhanced spontaneous emission from the NV center and allowed its position to be determined with greater spatial resolution.

The scanning qubit described here (Fig. 1) is a transmon design consisting of two aluminum islands connected by a thin aluminum wire interrupted by an aluminum oxide tunnel barrier²⁴. The tunnel barrier provides a large nonlinear inductance, which together with the capacitance between the two islands, makes the transmon behave as a nonlinear LC oscillator whose lowest two energy states can be used as a qubit. The transmon design is well suited for scanning because it couples to CPWRs capacitively and requires no physical connections. The qubit chip was mounted face down to a cryogenic three-axis positioning stage and positioned over a separate chip containing a niobium CPWR with a half-wave resonance at 7.6 GHz. In order to avoid direct contact between the resonator and the qubit, pads of photoresist 7 μm thick were deposited on the corners of the qubit chip. The sample holder was mounted to a dilution refrigerator which operated at temperatures ≤ 35 mK.

The main result presented here is the measurement of the strength g of the coupling between the resonator and the qubit as a function of qubit position. Following ref. 24, the Hamiltonian \hat{H} describing the coupled resonator-qubit system can be approximated by

$$\hat{H} = h\nu_r \left(\hat{a}^\dagger \hat{a} + \frac{1}{2} \right) + \frac{h\nu_q}{2} \hat{\sigma}_z + \frac{hg}{2} (\hat{a} \hat{\sigma}^+ + \hat{a}^\dagger \hat{\sigma}^-) \quad (1)$$

with ν_r and ν_q the resonator and qubit frequencies respectively. In this expression, \hat{a}, \hat{a}^\dagger are the creation and annihilation operators associated with photons in the resonator and $\hat{\sigma}^+, \hat{\sigma}^-,$ and $\hat{\sigma}_z$ are the Pauli spin matrices associated with the qubit when treated as a two-level system. On resonance ($\nu_q = \nu_r$), the first two excited states of the system are $(|0 \uparrow\rangle \pm |1 \downarrow\rangle)/\sqrt{2}$ with corresponding

energies $h\nu_r \pm hg$ above that of the ground state $|0 \downarrow\rangle$ where $|nq\rangle$ is the state with n photons in the resonator and the qubit in state q with \downarrow (\uparrow) representing the qubit ground (excited) state. When driven with a microwave excitation, transitions to each of these excited states are allowed, resulting in two peaks in the low power transmission spectrum. These peaks are separated in frequency by $2g$, called the vacuum Rabi splitting.

The frequency ν_r of the resonator depends on its capacitance to its ground plane which is decreased when the qubit chip is brought into close proximity. In order to ensure that resonance was possible at every qubit position, the qubit was fabricated with a pair of tunnel barriers integrated into a loop in place of a single tunnel barrier. By varying the flux through this loop with a magnet coil incorporated into the positioner, the qubit frequency ν_q could be varied from a maximum value of 12.1 GHz to close to zero²⁴. We note that, although here the flux loop's only purpose is to make the qubit energy tunable, such a loop can also be operated as a sensitive local magnetometer in a scanning SQUID microscope²⁵.

Fig. 2 shows the transmission spectra of the resonator for a sequence of regularly spaced qubit positions along the y axis perpendicular to the resonator. At each position, the current through the magnet coil was adjusted to bring the qubit into resonance, where the single transmission peak of the resonator was transformed into two peaks of equal height, clearly demonstrating strong coupling between the scanning qubit and the resonator. The position scan shows two regions of large peak separation symmetric about a position with nearly no peak separation which we set as the origin. In coupling to the resonator the transmon behaves as a dipole antenna. Because the two islands of the qubit are identical, by symmetry no coupling is expected when the qubit is centered above the resonator at $y = 0$. The points of maximum peak separation occur at $y \approx \pm 50 \mu\text{m}$ where one of the two islands is centered over the resonator. At these points, the observed coupling strength $g \approx 140$ MHz was well into the strong coupling regime $g > \kappa, T_1^{-1}$ where the qubit relaxation time $T_1 = 2.6 \mu\text{s}$ was determined by time-domain measurements (see Supplemental Methods) and the photon escape rate $\kappa = 13$ MHz was determined from the resonator linewidth. The photon escape rate was chosen to be large in order to increase the rate of data acquisition.

Scans of resonant transmission versus y position like Fig. 2 were repeated at five positions along the length of the resonator (the \hat{x} direction) with a spacing of 600 μm . The coupling strengths g extracted from fits to the transmission spectrum at each qubit position are plotted in Fig. 3. The coupling strength increases as the qubit moves from the voltage node at the center of the resonator to the antinode at its end but exhibits the same shape for its y dependence at each x position.

We now consider the data in Fig. 3 more quantita-

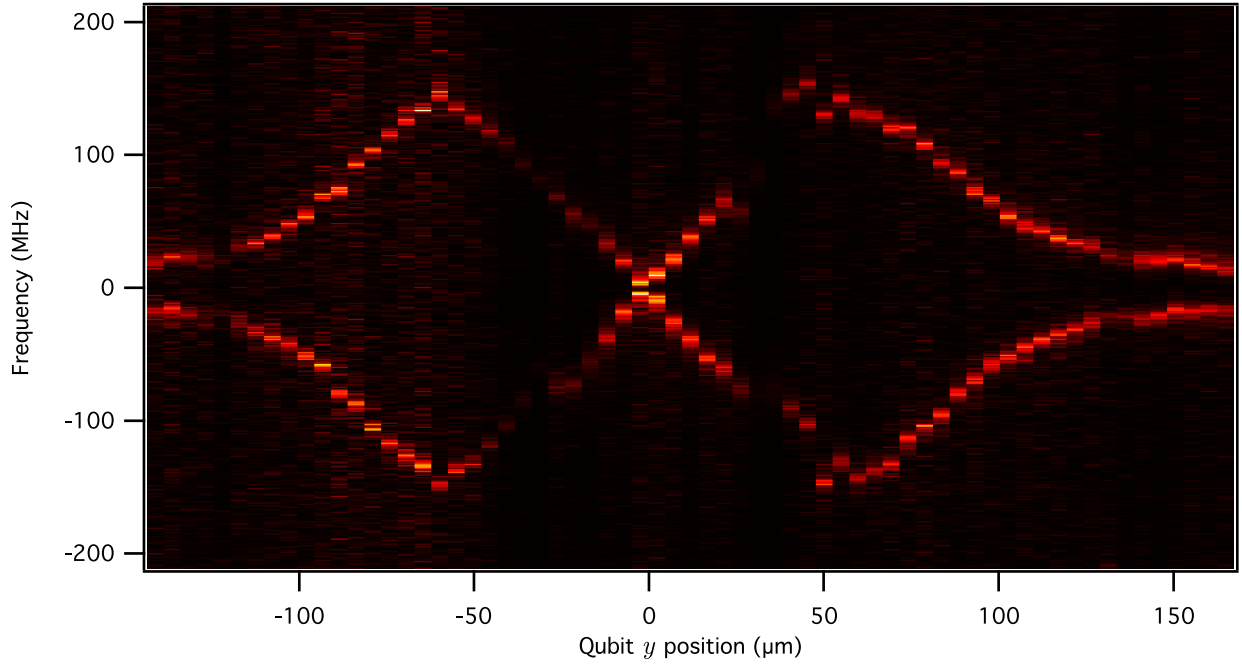


Figure 2. Resonant transmission spectra. Transmission spectra taken with the qubit in resonance with the resonator are shown for a series of qubit positions. The vertical axis represents the difference between the frequency of the applied microwave drive and the resonator frequency. The shifted peak locations can also be interpreted as values of the coupling strength g which is equal to the peak separation. We take the y origin to be the point of smallest peak separation which we interpret as the position where the qubit is centered over the resonator. The suppressed transmission at positions $y = \pm 30$ and $\pm 125 \mu\text{m}$ is due to coupling between the resonator and a parasitic resonance in the metal frame of the qubit chip (see Supplemental Discussion).

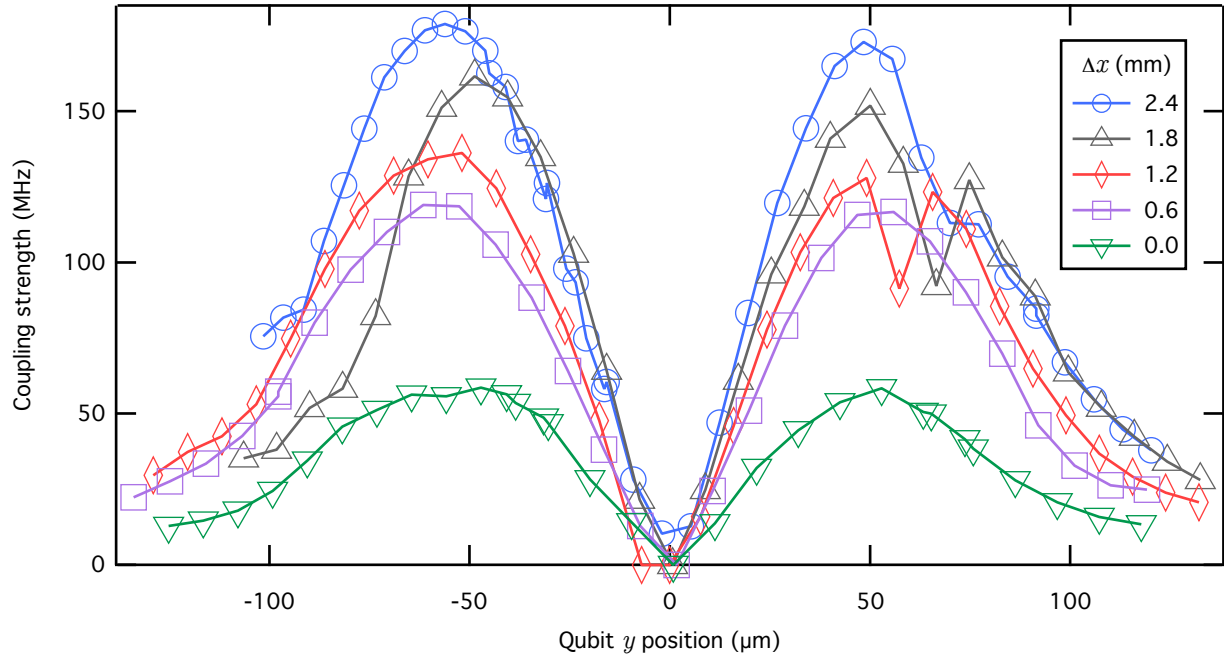


Figure 3. Coupling strength g versus qubit position. Traces of g versus qubit y position are shown for five qubit x positions spaced $600 \mu\text{m}$ apart from each other. The traces correspond to scans like the one shown in Fig. 2. Each value of g was determined by fitting several transmission spectra taken at values of magnetic flux for which the qubit frequency was close to that of the resonator. The sign of Δx was chosen so that with increasing Δx the qubit moved from the electric field node at the center of the resonator towards the electric field antinode at its end.

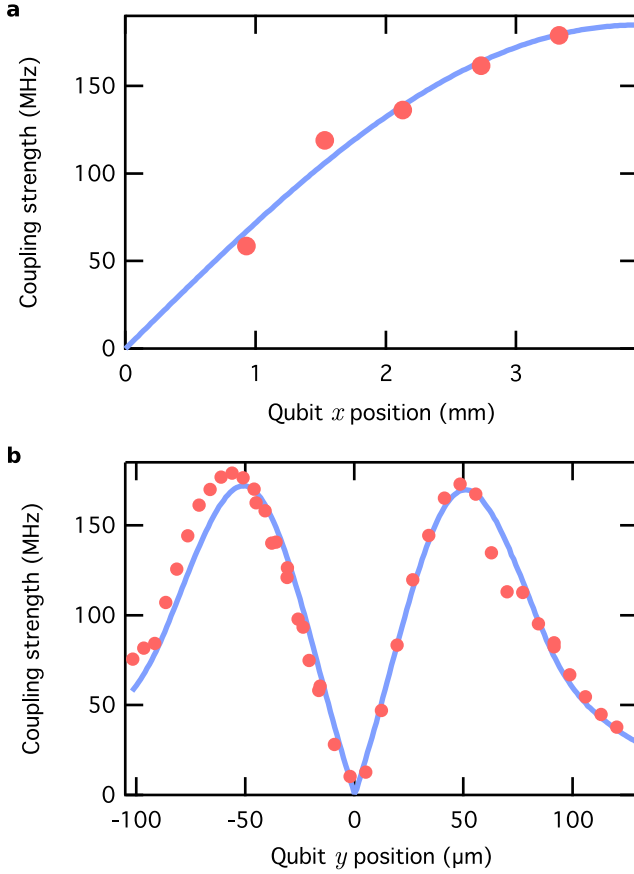


Figure 4. Quantitative analysis of measured coupling strength. **a**, The maximum coupling strength g of each trace in Fig. 3 is plotted versus x position along with a fit to the expected sinusoidal dependence. The x origin represents the midpoint of the resonator. The offset of the data points from the resonator midpoint was determined by the fit (see Supplemental Methods). The other fit parameter, the maximum coupling strength the end of the resonator, was found to be 185 MHz. **b**, The largest trace of g vs. y in Fig. 3 is replotted along with a fit to the form expected from finite element modeling of the qubit-resonator system’s capacitance matrix. The fitting function uses the resonator frequency ν_r , the system geometry, and the qubit x position determined in panel **a** as fixed inputs and treats the qubit height z , found to be 11 μm , as its only free parameter.

tively. The coupling strength g is proportional to the electric field at the position of the qubit when a single photon is present in the resonator. Panel **a** of Fig. 4 shows the maximum value of g for each x position along with a fit to the expected sinusoidal dependence of the electric field strength along the x direction. The fit provides an absolute reference for the relative x positions quoted in Fig. 3. With the x position known, we can compare the measurement data with the $g(x, y, z)$ obtained from finite element simulations (see Supplemental Methods). Panel **b** of Fig. 4 shows the values of g observed for $x = 3,330 \mu\text{m}$ from the resonator mid-

point along with the simulation results which show good agreement. The simulation height $z = 11 \mu\text{m}$ is somewhat larger than the 7 μm thickness of the photoresist pads on the corners of the qubit chip but corresponds to a misalignment between the qubit and resonator chips of $\sim 0.1^\circ$ over the 2 mm from the edge of the qubit chip to the qubit’s location at the chip center.

In conclusion, we have observed strong coupling between a scanning transmon qubit and a CPWR. Because strong coupling can be reached, anything possible with stationary qubits now becomes possible with a moveable probe opening the door for a wide array of applications in the field of CQED. Such a scanning qubit makes possible quantum measurements of superconducting circuits with spatial resolution. In addition to the scanning measurements of a lattice CQED system discussed earlier, we note that the system studied here demonstrates *in situ* tuning of the coupling strength g which is often a desirable capability experimentally. While the scanning qubit’s coupling can not be tuned on the timescale of the coherence time like some previously demonstrated circuit designs^{26, 27}, it does not require flux or current biasing of the system. For example, for the lattice CQED system mentioned above, a lattice of resonators on one chip could be coupled to a lattice of qubits on a second chip allowing the coupling between each resonator-qubit pair to be tuned together as one chip is scanned over the other. An array of qubits could also be used to measure the statistics of qubit coherence by scanning the qubits one by one across a single measurement resonator.

METHODS

The qubit was fabricated using electron beam lithography and double-angle shadow evaporation with controlled oxidation of 30 and 100 nm layers of aluminum onto a 4×4 mm sapphire chip. The 0.5×1.0 mm crashpads on the corners of the chip were made with photolithography of SU-8 2005 photoresist. The resonator was defined by photolithography and acid etch (H_2O , HF , and HNO_3 in a 7.5:4:1 ratio) of a 200 nm film of niobium on a 14×14 mm sapphire chip.

The qubit chip was glued with methyl methacrylate to the tip of a highly conductive copper rod mounted to the cryogenic positioning stage (Attocube ANPx340/RES, ANPz101/RES). The resonator chip was mounted to a copper patterned circuit board with silver paste and aluminum wire bonds which connected the input and output transmission lines to coaxial lines. Wire bonds were only placed around the edge of the chip outside the footprint of the qubit chip. The wiring scheme of the coaxial lines was the same as that described in ref. 28.

All values of qubit position were determined by potentiometric measurements of resistive position encoders integrated into the positioning stage. Individual position

readings had an uncertainty of $0.4\text{ }\mu\text{m}$, and overall the position readings drifted by $1.8\text{ }\mu\text{m}$ per $100\text{ }\mu\text{m}$. A typical movement of the positioning stage heated the refrigerator from its base temperature of $\lesssim 15\text{ mK}$ to over 85 mK . In order to reduce measurement time, most measurements were taken with the refrigerator in the range between 25 and 35 mK which took only a couple minutes to reach after moving the stage.

ACKNOWLEDGEMENTS

This work was supported by DARPA under grant #N66001-10-1-4023. DLU is supported by a fellowship from the NSF (DGE-1148900).

AUTHOR CONTRIBUTIONS

A. A. H. conceived and supervised the experiment. D. L. U. designed and built the sample holder and fabricated the samples. W. E. S. designed and fabricated the samples, performed the measurements and data analysis, and wrote the manuscript. All authors discussed the results and implications and commented on the manuscript at all stages.

COMPETING FINANCIAL INTERESTS

The authors acknowledge no competing financial interests.

* wshanks@princeton.edu

- [1] Bloch, I., Dalibard, J. & Nascimbène, S. Quantum simulations with ultracold quantum gases. *Nature Phys.* **8**, 267–276 (2012).
- [2] Blatt, R. & Roos, C. F. Quantum simulations with trapped ions. *Nature Phys.* **8**, 277–284 (2012).
- [3] Houck, A. A., Türeci, H. E. & Koch, J. On-chip quantum simulation with superconducting circuits. *Nature Phys.* **8**, 292–299 (2012).
- [4] Chiorescu, I. *et al.* Coherent dynamics of a flux qubit coupled to a harmonic oscillator. *Nature* **431**, 159–162 (2004).
- [5] Wallraff, A. *et al.* Strong coupling of a single photon to a superconducting qubit using circuit quantum electrodynamics. *Nature* **431**, 162–167 (2004).
- [6] Schoelkopf, R. J. & Girvin, S. M. Wiring up quantum systems. *Nature* **451**, 664–669 (2008).
- [7] Clarke, J. & Wilhelm, F. K. Superconducting quantum bits. *Nature* **453**, 1031–1042 (2008).
- [8] Martinis, J. M. Superconducting phase qubits. *Quantum Inf. Process.* **8**, 81–103 (2009).
- [9] Blais, A., Huang, R.-S., Wallraff, A., Girvin, S. M. & Schoelkopf, R. J. Cavity quantum electrodynamics for superconducting electrical circuits: An architecture for quantum computation. *Phys. Rev. A* **69**, 062320 (2004).
- [10] Greentree, A. D., Tahan, C., Cole, J. H. & Hollenberg, L. C. L. Quantum phase transitions of light. *Nature Phys.* **2**, 856–861 (2006).
- [11] Hartmann, M. J., Brandão, F. G. S. L. & Plenio, M. B. Strongly interacting polaritons in coupled arrays of cavities. *Nature Phys.* **2**, 849–855 (2006).
- [12] Angelakis, D. G., Santos, M. F. & Bose, S. Photon-blockade-induced Mott transitions and XY spin models in coupled cavity arrays. *Phys. Rev. A* **76**, 031805 (2007).
- [13] Greiner, M., Mandel, O., Esslinger, T., Hänsch, T. W. & Bloch, I. Quantum phase transition from a superfluid to a Mott insulator in a gas of ultracold atoms. *Nature* **415**, 39–44 (2002).
- [14] Hayward, A. L. C., Martin, A. M. & Greentree, A. D. Fractional quantum Hall physics in Jaynes-Cummings-Hubbard lattices. *Phys. Rev. Lett.* **108**, 223602 (2012).
- [15] Petrescu, A., Houck, A. A. & Le Hur, K. Anomalous Hall effects of light and chiral edge modes on the kagomé lattice. *Phys. Rev. A* **86**, 053804 (2012).
- [16] Bardyn, C.-E. & İmamoğlu, A. Majorana-like modes of light in a one-dimensional array of nonlinear cavities. *Phys. Rev. Lett.* **109**, 253606 (2012).
- [17] Underwood, D. L., Shanks, W. E., Koch, J. & Houck, A. A. Low-disorder microwave cavity lattices for quantum simulation with photons. *Phys. Rev. A* **86**, 023837 (2012).
- [18] Eriksson, M. A. *et al.* Cryogenic scanning probe characterization of semiconductor nanostructures. *Appl. Phys. Lett.* **69**, 671–673 (1996).
- [19] Topinka, M. A. *et al.* Imaging coherent electron flow from a quantum point contact. *Science* **289**, 2323–2326 (2000).
- [20] Johnson, B. R. *et al.* Quantum non-demolition detection of single microwave photons in a circuit. *Nature Phys.* **6**, 663–667 (2010).
- [21] Rondin, L. *et al.* Nanoscale magnetic field mapping with a single spin scanning probe magnetometer. *Appl. Phys. Lett.* **100**, 153118 (2012).
- [22] Maletinsky, P. *et al.* A robust scanning diamond sensor for nanoscale imaging with single nitrogen-vacancy centres. *Nat. Nanotechnol.* **7**, 320–324 (2012).
- [23] Englund, D. *et al.* Deterministic coupling of a single nitrogen vacancy center to a photonic crystal cavity. *Nano Lett.* **10**, 3922–3926 (2010).
- [24] Koch, J. *et al.* Charge-insensitive qubit design derived from the Cooper pair box. *Phys. Rev. A* **76**, 042319 (2007).
- [25] Huber, M. E. *et al.* Gradiometric micro-SQUID susceptometer for scanning measurements of mesoscopic samples. *Rev. Sci. Instrum.* **79**, 053704 (2008).
- [26] Bialczak, R. C. *et al.* Fast tunable coupler for superconducting qubits. *Phys. Rev. Lett.* **106**, 060501 (2011).
- [27] Srinivasan, S. J., Hoffman, A. J., Gambetta, J. M. & Houck, A. A. Tunable coupling in circuit quantum electrodynamics using a superconducting charge qubit with a V-shaped energy level diagram. *Phys. Rev. Lett.* **106**, 083601 (2011).

[28] DiCarlo, L. *et al.* Demonstration of two-qubit algorithms with a superconducting quantum processor. *Nature* **460**, 240–244 (2009).

SUPPLEMENTARY METHODS

Fitting functions

Non-linear least-squares fitting routines were used to determine the coupling strength g from transmission data and to produce the curves shown in Fig. 4. Here we briefly describe the functions used in each case.

$$|\pm\rangle = \frac{\frac{\Delta}{2} \pm \sqrt{\left(\frac{\Delta}{2}\right)^2 + g^2}}{\sqrt{g^2 + \left(\frac{\Delta}{2} \pm \sqrt{\left(\frac{\Delta}{2}\right)^2 + g^2}\right)^2}} |0 \uparrow\rangle + \frac{g}{\sqrt{g^2 + \left(\frac{\Delta}{2} \pm \sqrt{\left(\frac{\Delta}{2}\right)^2 + g^2}\right)^2}} |1 \downarrow\rangle$$

and

$$\nu_{\pm} = \frac{\nu_r + \nu_q \pm \sqrt{4g^2 + \Delta^2}}{2} \quad (\text{S1})$$

with $\Delta = \nu_q - \nu_r$. The peak amplitudes are proportional to the probabilities $w_{\pm} = |\langle 1 \downarrow | \pm \rangle|^2$ of a photon being measured in the states $|\pm\rangle$. The peak linewidths γ_{\pm} are equal to the decay rates of the qubit (T_1^{-1}) and the photon (κ) weighted by the probability of measuring a qubit excitation and a photon respectively: $\gamma_{\pm} = w_{\pm}\kappa + (1 - w_{\pm})T_1^{-1}$. We take transmission peaks as following a lorentzian lineshape and use the following form to fit the resonator transmission:

$$S_{21}(\nu) = B + A \left| \sum_{\pm} w_{\pm} l(\nu, \nu_{\pm}, \gamma_{\pm}) \right|^2 \quad (\text{S2})$$

where A is the overall amplitude accounting for all attenuation and amplification in the measurement circuit, B is the background of the detector, and $l(\nu, \nu_0, \gamma)$ is the complex lorentzian centered at ν_0 with width γ :

$$l(\nu, \nu_0, \gamma) = \left(1 - i \frac{\nu - \nu_0}{\gamma/2} \right)^{-1}.$$

When fitting for g , the parameters A , B , κ , ν_q , ν_r , and g were allowed to vary, while T_1 was held fixed to the value obtained from coherence measurements. Fig. S1 shows the result of fitting one of the transmission spectra from Fig. 2. Also shown is a plot of transmission versus flux as the qubit passes through resonance. For the coupling strength values shown in Fig. 3, similar flux scans were taken and the plotted values of coupling strength were

Transmission measurements

Transmission measurements were made in the low power limit for which the rate of photons entering the resonator was less than the escape rate, so that the resonator occupancy was less than one photon on average. In this case, the transmission spectrum contains peaks at frequencies ν_{\pm} corresponding to transitions from the ground state $|0 \downarrow\rangle$ to the states $|+\rangle$ and $|-\rangle$ which possess a $|1 \downarrow\rangle$ component and are located at energies $h\nu_+$ and $h\nu_-$ above the ground state. The states and their frequencies are found by diagonalizing the Hamiltonian given in equation (1):

obtained by averaging the coupling strength values obtained from fitting the transmission at each flux value.

Coupling strength versus x

The voltage profiles of the modes of a CPWR with open boundary conditions are sinusoidal along the length of the resonator with antinodes at its ends. The coupling strength is proportional to the resonator voltage with one photon present and so should follow this sinusoid. The maximum coupling strength at each x position shown in panel **a** of Fig. 4 was fit to the sinusoidal form:

$$g(\Delta x) = g_{\max} \sin \left(\pi \frac{\Delta x + x_0}{l_r} \right) \quad (\text{S3})$$

where $l_r = 7,872 \mu\text{m}$ is the resonator length and g_{\max} and x_0 were the fitting parameters. Here Δx is the set of displacements in x from the first x position (i.e. the values are $0 \mu\text{m}$; $600 \mu\text{m}$; $1,200 \mu\text{m}$; etc.). In panel **a** of Fig. 4, the measured coupling strengths and the fit are plotted versus $x = \Delta x + x_0$.

Coupling strength versus y

In order to perform the fit of coupling strength versus y shown in panel **b** of Fig. 4, the following expression for the coupling strength given in ref. 24 was used:

$$g(x, y, z) = 2\sqrt{\frac{2Z_c}{h}} m(x) \nu_r \beta(y, z) n_{01}(y, z, \nu_r)$$

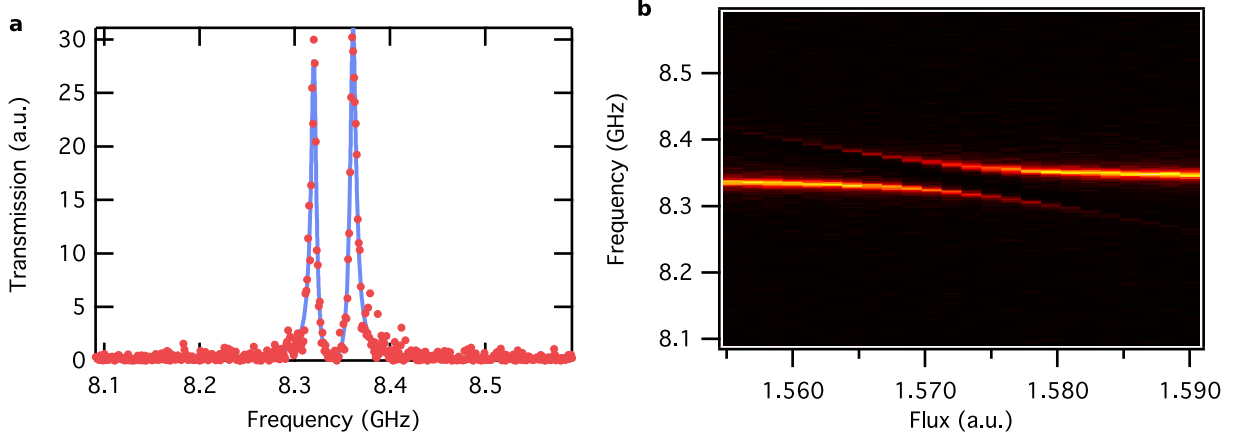


Figure S1. Fitting resonator transmission. **a**, The transmission at $y = 146 \mu\text{m}$ in Fig. 2 is plotted in arbitrary units along with a fit to equation (S2). The fit coefficients are $A = 57$, $B = 0.2$, $g = 20 \text{ MHz}$, $\kappa = 14 \text{ MHz}$, $\nu_r = 8.342 \text{ GHz}$, and $\nu_q = 8.339 \text{ GHz}$. **b**, Transmission spectra recorded at the same position as panel **a** are plotted versus flux in arbitrary units as the qubit passes through resonance. Averaging the coefficients from fits to the transmission at each flux value gives $A = 59 \pm 3$, $B = 0.30 \pm 0.05$, $g = 20.4 \pm 0.3 \text{ MHz}$, $\kappa = 12.8 \pm 0.8 \text{ MHz}$, and $\nu_r = 8.342 \pm 0.001 \text{ GHz}$ where the errors represent the standard deviation of the coefficients.

with the characteristic line impedance Z_c taken to be 50Ω and $m(x)$ the sinusoidal mode shape factor given in equation (S3). In order to describe the voltage division factor β and the transmon matrix element n_{01} , we first define C_{jk} to be the capacitance between components j and k and label the components of the system with a and b for the two islands of the transmon, p for the resonator center pin, and g for all other pieces of metal (the two ground planes and the metal frame on the qubit chip). The voltage division factor β gives the fraction of the voltage drop from the resonator center pin to ground that falls across the two islands of the qubit. It can be written in terms of capacitance coefficients as

$$\beta = \frac{|C_{ap}C_{bg} - C_{bp}C_{ag}|}{C_{ab}(C_{a\Sigma} + C_{b\Sigma}) + C_{a\Sigma}C_{b\Sigma}}$$

where $C_{x\Sigma} = C_{xp} + C_{xg}$. We find the matrix element n_{01} by numerically diagonalizing the transmon Hamiltonian given in ref. 24

$$\hat{H} = 4E_C \hat{n}^2 - E_J \cos \hat{\varphi}$$

to find its eigenstates and eigenenergies and then evaluating $n_{01} = \langle 0 | \hat{n} | 1 \rangle$, where $|0\rangle$ and $|1\rangle$ are the eigenstates with the two lowest energies, E_0 and E_1 . The charging energy $E_C = e^2/2C_\Sigma$ used in the calculation was calculated using the total capacitance given by

$$C_\Sigma = C_{ab} + \left(\frac{1}{C_a} + \frac{1}{C_b} \right)^{-1}.$$

The qubit frequency ν_q is given by $(E_1 - E_0)/h$ and is thus a function of E_C and E_J . In calculating n_{01} , $\nu_q(E_C, E_J)$ was numerically inverted to solve for $E_J(E_C, \nu_q)$ with

ν_q set equal to ν_r since measurements of the coupling strength were made with the qubit close to the resonator's frequency.

In order to produce the fit shown in panel **b** of Fig. 4, the coupling strength $g(x, y, z)$ was calculated using the known values of Z_c and ν_r , the value of x obtained from the fit in panel **a** of Fig. 4, and the values of the capacitances C_{jk} found by finite element analysis for a grid of y and z values with $1 \mu\text{m}$ spacing. The measured coupling strength versus y was fit to the $g(y, z)$ found by interpolating between the y and z grid points with z as the only free parameter. The finite element simulation was then repeated with the fitted value of z in order to produce the curve shown in panel **b** of Fig. 4. We note that at the fitted value of $z = 11.0 \mu\text{m}$ the charging energy $E_C = 388 \text{ MHz}$ is similar to values used in other CQED experiments and corresponds to a ratio of $E_J/E_C = 59$, within the transmon regime where the offset charge across the transmon islands (not included in the Hamiltonian given above) may be ignored.

By the use of alignment marks on the resonator and qubit chips, it was possible to confirm that the misalignment between the two chips was $3^\circ \pm 1^\circ$. A misalignment of 3° was used in the finite element calculations for the capacitance coefficients. Using a misalignment of 2° (4°) instead gave a fitted height z of $11.1 \mu\text{m}$ ($10.7 \mu\text{m}$).

Coherence measurements

Qubit coherence times ($T_1 = 2.6 \pm 0.3 \mu\text{s}$, $T_2^* = 1.0 \pm 0.2 \mu\text{s}$) were obtained using the techniques described in ref. 29. The measurements were made during the same cooldown and at the same x position as the data shown

in Fig. 2. For technical reasons, the measurements were made immediately after the refrigerator was warmed up to 20 K and then cooled back down to its base temperature. The coherence measurements were performed at $y = -113 \mu\text{m}$ ($g = 31 \text{ MHz}$) in Fig. 2 with the qubit frequency detuned 700 MHz below the resonator.

SUPPLEMENTARY DISCUSSION

Here we provide some additional measurements and analysis related to scanning the qubit over the resonator. In Fig. 2, the transmission is suppressed near $y = \pm 30$ and $\pm 125 \mu\text{m}$ due to the resonator's coupling to spurious modes. Because the behavior of these modes is symmetric in qubit position, we believe them to be caused by resonances between the resonator chip and a layer of metal on the qubit chip that was patterned symmetrically. The extra metal on the qubit chip was deposited for technical reasons and is not needed for the functioning of the qubit. By redesigning the qubit chip or resonator chip, these modes could be eliminated.

In panel **a** of Fig. S2, the data from Fig. 2 is replotted after removing the background and normalizing the transmission peaks to unity in order to make the peaks near $y = \pm 30$ and $\pm 125 \mu\text{m}$ more visible. In Fig. 2, the origin of the frequency axis was set to the location of the high power transmission peak and the qubit frequency was tuned to produce two peaks of equal height in transmission. For some positions near where the resonator coupled to the spurious modes, these conditions produced two peaks not centered around zero. In panel **a** of Fig. S2, the frequency axis at each position has been shifted to center the peaks around zero, so that the transmission peaks at neighboring positions can be more easily compared.

The spurious modes appeared as lower and broader peaks in transmission at frequencies that varied with position and did not vary with magnetic flux. These modes were always present but only affected the measurement of the resonator-qubit system when their frequencies were close to the resonator frequency. When the frequency of one of these modes was close to the resonator frequency, the coupling between the spurious mode and the resonator resulted in two modes with excitations partially of the resonator and partially of the spurious mode. The narrower peak of the resulting two peaks in transmission was chosen to be the resonator peak for the purpose of coupling to the qubit. Panel **b** of Fig. S2 shows the frequency of the chosen peak for each position in Fig. 2. Jumps in the resonator frequency due to avoided crossings with spurious modes are visible at the y positions with low transmission in Fig. 2.

The scan shown in Fig. 2 was taken on a separate cooldown from the scans shown in Fig. 3. The same resonator and qubit samples were used for both sets of

measurements, but the sample stage was disassembled in between the cooldowns. During the cooldown in which data in Fig. 2 was taken, the qubit's x position was not varied, so the absolute x position of the data is not known. However, using the maximum value of g from Fig. 2 and the curve shown in panel **a** of Fig. 4 to calibrate the x position, one finds the data in Fig. 2 was taken at $x = 2,116 \mu\text{m}$.

Changing the position of the qubit also affected the threading of flux through the qubit's SQUID loop. Once the SQUID loop was moved away from the gaps in the coplanar waveguide and positioned above the superconducting ground plane, the amount of flux produced by the magnet coil required to tune qubit into resonance increased rapidly because the Meissner effect screened the magnetic field away from the superconducting ground plane. In panel **c** of Fig. S2, the coil magnetic flux that brought the qubit into resonance with the resonator is plotted for each position of Fig. 2. The impact of the magnetic field screening could be greatly reduced by fabricating holes in the resonator's ground plane.

The strong dependence of the resonant magnetic flux on the qubit position as well as the steepness of the slope of qubit frequency versus magnetic flux (maximum qubit frequency $\nu_{q,\text{max}} \sim 12.1 \text{ GHz}$) necessitated careful flux scanning at each qubit position in order to locate resonance. Searching for resonance by monitoring the transmission spectrum for an avoided crossing feature like the one shown in panel **b** of Fig. S1 would have required a long measurement time at each qubit position. Instead, only the low power transmission at the frequency ν_r of the high power transmission peak was monitored as the flux was swept.

When $|\nu_r - \nu_q| \gg g$, one of the two mode frequencies ν_{\pm} given in equation (S1) differs from ν_r by $\sim g^2/(\nu_r - \nu_q)$ and is associated with a large peak in transmission. For most qubit frequencies this frequency shift is small compared to the resonator linewidth $\kappa = 13 \text{ MHz}$ and so transmission at ν_r is high. However, when $\nu_q \sim \nu_r$, the mode frequencies ν_{\pm} are shifted from ν_r by $g > \kappa$ and transmission at ν_r is low. Panel **a** of Fig. S3 illustrates this behavior by showing transmission at ν_r versus flux and input power. Regular dips in transmission occur at low power where the qubit passes through resonance. Panel **b** of Fig. S3 plots just the low power transmission versus flux and shows that resonance can be easily identified by monitoring transmission at just one frequency value. In practice, a scan like that shown in panel **b** was taken at each position to identify the resonant flux range, and then a scan like that shown in panel **b** of S1 was taken over this flux range to obtain transmission spectra to fit for g .

Additional features are present in the crossover from the low power region to the high power region of the transmission. Panel **c** of S1 shows a finer scan of transmission versus power and flux at a qubit position close

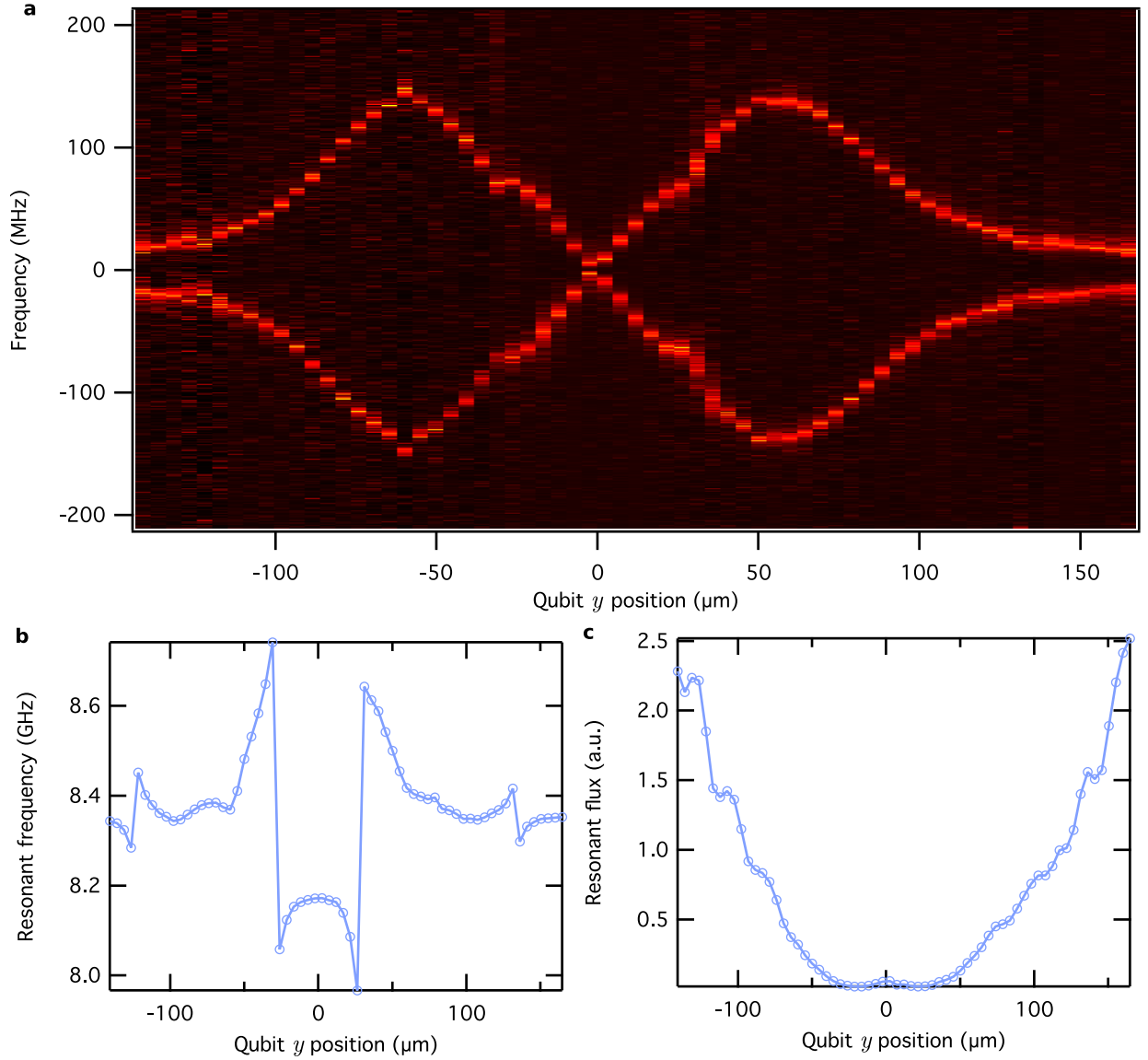


Figure S2. Additional information about Fig. 2. **a**, The transmission spectra with the qubit tuned into resonance with the resonator is plotted for a series of qubit positions. At each position, the background is removed and the transmission is scaled so that the maximum transmission is unity. The frequency of each spectrum is offset so that the two peaks are centered around zero. **b**, The resonator frequency is plotted for each qubit position of Fig. 2. The frequency axis of each spectrum in Fig. 2 was offset by the frequency plotted here. **c**, The total flux (in arbitrary units) sourced by the magnet coil to bring the qubit into resonance is plotted versus qubit position for the scan shown in Fig. 2.

to that of the scan in panel **a**. These features are likely related to higher level qubit transitions coming into resonance with the resonator, though additional analysis is needed.

In the main text, results have been presented for the coupling of the qubit to the resonator as a function of lateral position (x and y). Measurements of the coupling's dependence on the qubit's vertical displacement z from the resonator were not possible due to misalignment between the resonator and qubit chips. Evidence of this misalignment is visible in panel **a** of Fig. S3 which plots

the resonator frequency versus the positioner's z reading denoted by z_p . The origin of z_p was chosen to be the point at which the positioner could no longer advance due to contact with the resonator chip. Above $z_p = 40 \mu\text{m}$, the resonator frequency is shifted to higher values as the qubit chip is brought closer as expected due to the modification of the resonator's effective dielectric constant by the qubit's presence. Below $40 \mu\text{m}$, the resonator frequency's dependence on z_p weakens and disappears even as the positioner continues to move. We interpret this behavior as the qubit chip coming into first partial con-

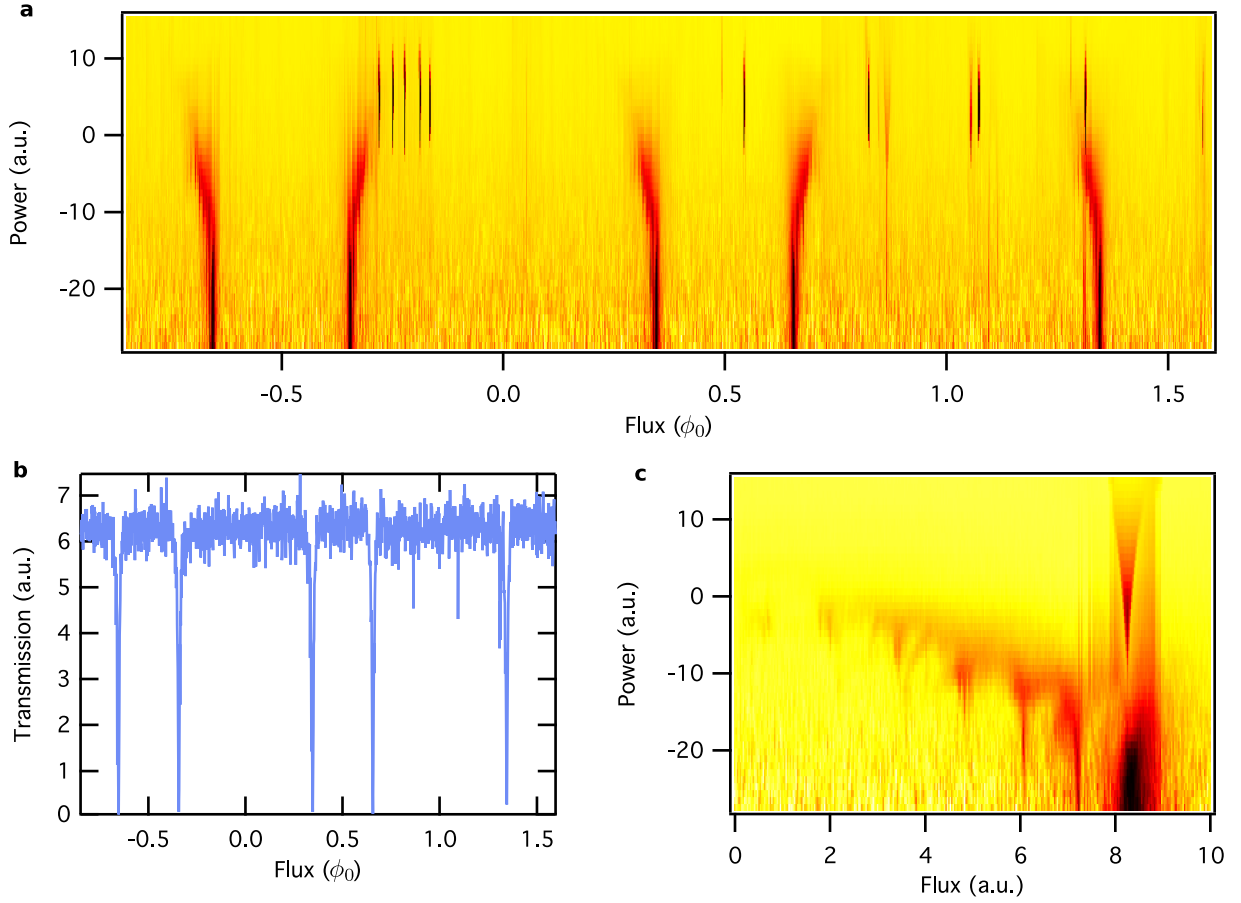


Figure S3. Transmission at the resonator frequency versus input power and magnetic flux. **a**, The transmission at ν_r is plotted versus input microwave power on a log scale and magnetic flux threading the qubit loop. The flux axis has been scaled by the observed flux period ϕ_0 . The power axis is uncalibrated, but the cross-over near -15 on resonance occurs as the photon occupation of the resonator increases from 0.1 to 10. The scan was taken at the same x position as Fig. 2 with the qubit close to the center pin and $g = 29$ MHz. **b**, The average of the transmission for powers less than -19 in panel **a** is plotted versus flux. **c**, Another scan of transmission versus power and flux like that in panel **a** is plotted for a flux region close to resonance. The flux axis is uncalibrated. The scan was taken at a position with $g = 21$ MHz, close to the position used for the scan shown in panel **a**.

tact with the resonator and then nearly full contact as compliance in the sample holder allow the two chips to align. We attribute the relatively small magnitude of the discrepancy of the qubit height obtained by the fit shown in Fig. 4 from the height of the photoresist pads to this compliance in the sample holder.

We note that the shift of the resonator frequency due to the qubit chip shown in panel **a** of Fig. S4 demonstrates the possibility of using a scannable chip to produce a defect in a CQED lattice by shifting the frequency of one of the resonators within the lattice. For scanning experiments where no defect is desired, the shift shown in panel **a** could be made unimportant by scanning with a chip larger than the entire CQED lattice. In this case, the resonator at each lattice site would receive the same shift.

The resonator frequency's dependence on the qubit

chip height shown in panel **a** of Fig. S4 allowed the resonator to be used to measure the qubit height. Panel **b** of Fig. S4 plots noise spectra of the transmitted phase at the resonator frequency when the qubit chip is at $z_p = 0$ and $43 \mu\text{m}$. We interpret the phase fluctuations present when the qubit chip is hovering above the resonator and not present when the qubit chip is in hard contact as being due to motion of the qubit chip relative to the resonator chip. Using the resonator's phase versus frequency curve to convert the phase noise into an effective resonator frequency noise and then the curve shown in panel **a** of Fig. S4 to convert frequency into position, we obtain the position noise spectrum shown in panel **c** of Fig. S4. Repeating this procedure at another z_p position and using the amplitude noise instead of the phase noise resulted in vibration spectra with similar features at similar magnitudes, confirming the interpretation of

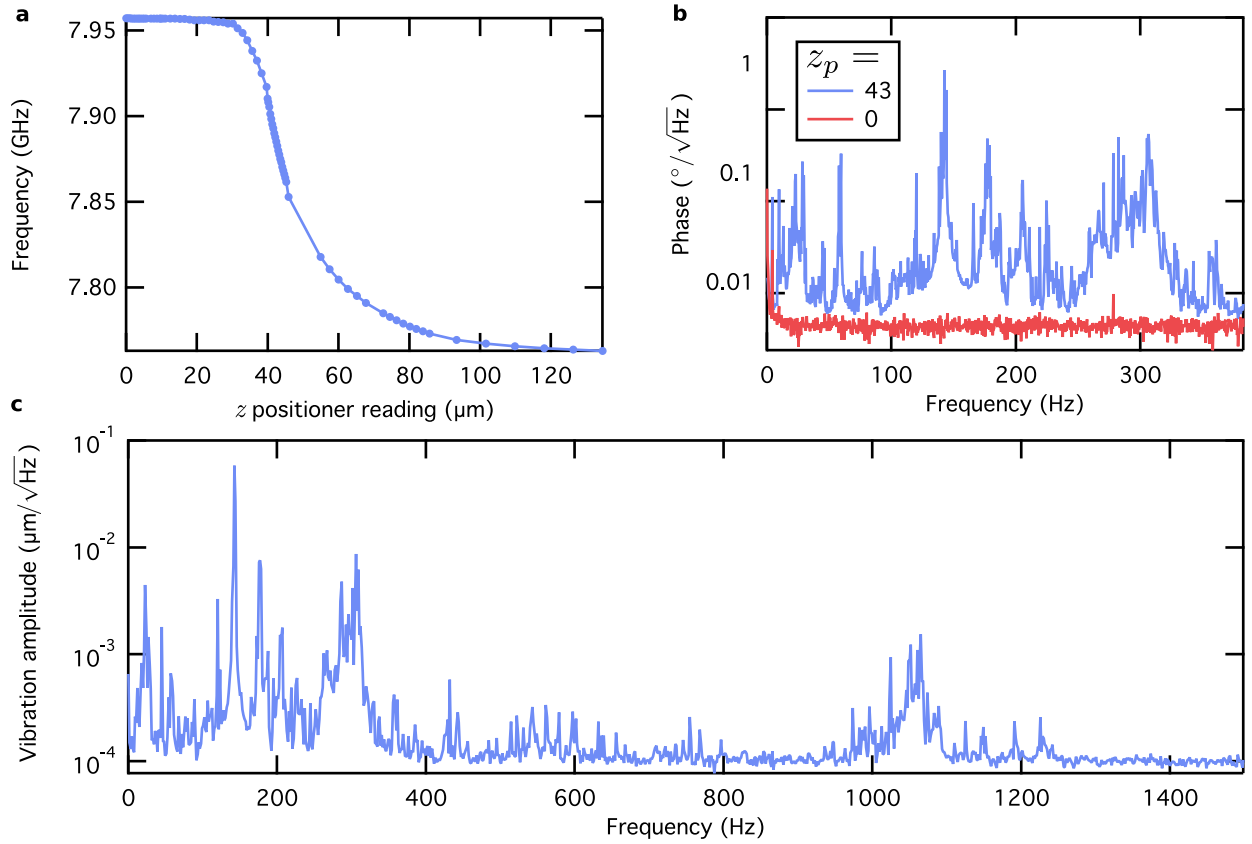


Figure S4. The effects of retracting the qubit from the resonator chip. **a**, The resonator frequency is plotted versus the reading z_p of the z positioner. At $z_p = 0$, the qubit chip is in hard contact with the resonator chip and can not be advanced further. **b**, The noise spectrum of the transmitted phase at the resonator frequency ν_r is plotted for the positions $z_p = 0$ and $43 \mu\text{m}$. **c**, The noise spectrum of the qubit-resonator displacement is plotted for $z_p = 43 \mu\text{m}$ using the data from panel **b**. The slope of the curve shown in panel **a** was used to convert the phase data into displacement.

the features as being due to vibration of the qubit chip. The spectrum shown in panel **c** of Fig. S4 is typical for the mechanical response of cryogenic positioners such as those used in this experiment. The motion of the refrigerator base plate inferred from the spectrum shown in panel **c** of Fig. S4 agreed with measurements made with an accelerometer of another refrigerator that was the same model as that used for the measurements presented here. Because all measurements of the qubit were made with the resonator and qubit chips in hard contact, no vibration isolation elements were included in the sample holder. In order to measure the dependence of

the qubit-resonator coupling on height, such vibration isolation would need to be considered in addition to the alignment of the qubit and resonator chips.

* wshanks@princeton.edu

[29] Schreier, J. A. *et al.* Suppressing charge noise decoherence in superconducting charge qubits. *Phys. Rev. B* **77**, 180502 (2008).